Imaging the Ethiopian Rift region Using Transdimensional Hierarchical Seismic Noise Tomography

Addis Eshetu [1,2], Tilahun Mammo[1] and Frederik Tilmann[3,4]

[1]School of Earth Sciences, Addis Ababa University, Addis Ababa, Ethiopia

[2]Department of Mathematics, Wolkite University, Wolkite, Ethiopia

[3]Deutsches GeoForschungsZentrum GFZ, Telegrafenberg, 14473 Potsdam, Germany

[4]Department, of Geosciences, Freie Universität Berlin, Berlin, Germany

Abstract

The Ethiopian rift is a unique natural environment to study the different stages of evolution from initial continental rifting to embryonic sea-floor spreading. We used transdimensional hierarchical Bayesian seismic ambient noise tomography to first construct group velocity maps across the Afar, Main Ethiopian Rift and the adjoining plateaus, and then inverted these for a shear wave velocity model. The uppermost mantle shear wave velocity ranges between 3.9 and 4.3 km/s, 5 – 15 % lower than the upper mantle velocity in the PREM model. The combined effect of temperature and partial melt is needed to explain a 15% shear wave velocity reduction in the uppermost mantle. Tectonic and magmatic activities are not localized to the rift center, but are widespread within the upper crust beneath the Main Ethiopian Rift and Afar. The Main Ethiopian Rift is dominated by two velocity belts, the Wonji Fault Belt along the rift axis and the Silti-Debre Zeit Fault Zone on the western side of the Central Main Ethiopian Rift; the Boru-Toru structural high appears to serve as a transfer zone between them, exhibiting relatively high crustal velocities (3.6 km/s) at 14 km depth. Low velocities persist in the crust beneath the rift flanks and border faults, indicating that they are still tectonically and magmatically active. The crust beneath the western plateau is characterized by a low velocity anomaly, implying that the plateau is also active. Low velocity linear belts are further imaged beneath the western and eastern plateaus, away from the active rift axes. These off-axis belts could represent failed or buried rifts.

1. Introduction

The Ethiopian Rift system, the northernmost part of the East African Rift System, is a seismically and volcanically highly active region, which is stretching and fragmenting Archean-Proterozoic continental lithosphere (Acocella et al., 2008) (Figure 1). It therefore provides a unique natural environment to study the different stages of evolution from continental rifting to embryonic sea-floor spreading (Woldegabriel et al., 2000; Yirgu et al., 2006; Keranen and Klemperer, 2008). The initiation of rifting is thought to have been triggered by the impingement of the Afar plume at the base of the lithosphere at ~31 Ma. The resultant domal uplift pattern affected the Northwestern Plateau, Afar and Yemen (White and Mckenzie, 1989). As a result ~900,000 km^3 of flood basalts were erupted (Rochette et al., 1998; Sembroni et al., 2016), locally reaching a thickness of up to 2 km and covering a surface area of about 600,000 km^2 in total (Mohr, 1983; Mohr and Zanetin, 1988; Rooney et al., 2007). 94% of the total volume lies in Ethiopia (84% in the western and 10% in the eastern plateaus), with the remaining 6% in Yemen. Most of the sequences erupted in a space of 1m.y. (Hofmann et al., 1997).

The volcanism in Ethiopia initiated during the Oligocene and continues to the present (Peccerillo et al., 2007; Merla et al., 1979; Kazmin et al., 1980; Kurkura, 2010; Ayalew, 2011). All eruption cycles were preceded and followed by episodes of rifting (Mohr, 1970; Kazmin et al., 1980; Mohr and Zanetin, 1988; Peccerillo et al., 2007). Pre-existing lines of weakness might have played a significant role in defining the position of the rifts. Rift evolutions and tectonic developments in Afar, Main Ethiopian Rift (MER) and the adjoining plateaus are complex and different stages of the breakup processes are involved.

Several competing hypotheses have been advanced for the spatio-temporal evolution of rifting. Northward propagation of rifting has been proposed by Woldegabriel et al., (1990) and Wolfenden et al., (2004). They suggested that the initial rifting began ~25 Ma in Kenya, followed by extension in the southern MER (SMER) and central MER (CMER) at ca. 18-15 Ma and finally the formation of the northern MER (NMER) commenced at ~11 Ma (Ebinger and Casey, 2001; Abbate et al., 2015). On the other hand, Buck (2006) and Rogers (2006) proposed southward propagation of rifting after initiation in Afar. A compromise is offered by Bonini et al., (2005) and Keranen and Klemperer (2008) with their hypothesis of the diachronous-in-space-and-time rifting model, in which rifting began more or less contemporaneously both in Afar (25-20 Ma) and in the SMER (21-20 Ma) with both rift propagating in the opposite directions. In this hypothesis, rifting propagated into the NMER at ~11 Ma. The southwest propagation of the NMER was temporarily checked and diverted to take the westward course along the Yerer-Tullu-Welel Volcano Tectonic Lineament (YTVL) (Keranen and Klemperer, 2008), which represent a system of EW transversal faults (Abebe et al., 1998). Around 5 Ma (Macgregor, 2015) the extension direction regained its original trend but with a slight rotation of the stress field to form the CMER (Keranen and Klemperer, 2008). A fourth model proposed by Rooney et al., (2007) considers the MER as the unification place of two rift systems – the Wonji Fault Belt (WFB) representing the Red Sea- related deformation, which propagates through Afar into the NMER, and the Silti–Debre Zeit Fault Zone (SDZF) representing the northward propagation of the East African-related deformation through SMER. The WFB eventually broke through the Boru Toru Structural High (BTSH) and started interacting with SDZF.

In this paper, we measure interstation Rayleigh group velocities in the Ethiopian rift region and its flanking plateaus and invert them for a three-dimensional shear wave model of the crust and upper mantle with a hybrid approach, which combines transdimensional hierarchical Bayesian group velocity tomography with linearized 1D inversion. Ambient noise tomography was first applied in Ethiopia by Kim et al., (2012) in the Main Ethiopian Rift (MER) and by Korostelev et al., (2015) in Afar; these works report the presence of magmatic activity beneath the MER and rift flank, respectively. More recently, Chambers et al., (2019) included both MER and Afar in their model and found low uppermost mantle shear velocities compared to the global average. Studies conducted by Kim et al., (2012) and Korostelev et al., (2015) are limited to specific regions (i.e. on the MER and Afar respectively) and do not give the general tectono-magmatic picture of the entire region. Chambers et al., (2019) used the conventional regularization approach.

Here, we combine all open datasets acquired over the region extending from the southern MER (SMER) to the northern Afar, including parts of the western and eastern plateaus. The Rayleigh wave group velocity maps are used to derive the 3D shear velocity structure of the crust and the upper mantle; the resulting models show more detail than previous geophysical studies, resolving anomalies ~50 km wide across nearly all of the study region,

and anomalies as small as 25 km in selected areas with high station density. Our results enabled us to expand our knowledge of magmatic processes during continental breakup and to explore the extent of crustal modification, inherent controlling structures and transitional zones within and across the Ethiopian rift.

2. Data and Method

2.1. Ambient noise analysis

We used continuous recordings of noise fields on 180 temporary and permanent broadband seismic stations operated in Ethiopia between 2000 and 2011 (Figure 1). During 2000-2002 seismic data were collected by the Ethiopian Broadband Seismic Experiment (EBS) (Nyblade, 2000). The Ethiopia Afar Geoscientific Lithospheric Experiment (EAGLE) phase I network was deployed between 2001 and 2003 (Maguire and SEIS-UK, 2002) and EAGLE phase II from 2002-2003 (Maguire et al., 2003). The Afar Consortium network deployed during 2007-2009 (Stuart et al., 2011); AFAR0911 seismic stations were operational during 2007-2009 (Keir and Hammond, 2009); the Afar Dense Array deployed from 2009-2011 (Gao, 2009). Additional data were sourced from two permanent stations: FURI (IRIS/USGS) (USGS, 1988) and DESE (Penn State University, 2004).

The first stage is the pre-processing of single station waveform data. The original continuous data recorded at each broadband seismic station were cut into 24-hour long data segments. The data were then re-sampled to two samples per second and the instrumental response, mean and trend were removed. The data were then passed through a second order butterworth bandpass filter between 0.025 and 1 Hz. Time domain one-bit normalization was applied to reduce the effects of earthquakes, instrumental irregularities and strong but intermittent noise sources near the stations, which can otherwise dominate the noise correlation function (Campillo and Paul, 2003; Shapiro and Campillo, 2004; Dias et al., 2015). Finally, spectral normalization was performed to whiten the amplitude spectrum to unit value without changing the phase of the signal.

Following single station data processing, daily cross-correlations were computed and stacked for each station pair to generate the empirical Green's functions (EGFs). In order to obtain reliable estimates, however, homogenously distributed noise sources are required. This is approximated by averaging the daily cross-correlations for as long as possible. In this study EGFs of more than 16,000 pairs were calculated from the 180 broadband stations. Of these, 2648 pairs were selected for further processing based on their signal to noise ratio and an assessment of the general appearance of the EGFs, as judged by visual inspection.

The reconstructed EGFs for all station pairs with good signal to noise ratio are shown in Figure 2. Rayleigh waves emerged with clear moveout. For most pairs, the signal-noise ratio on causal and anti-causal legs differed strongly, so that we simply selected the better of the two for making the group dispersion measurement. Apart from the dominant signal of the presumed surface wave, another phase is also detected at small lag times and with a moveout velocity of ~20 km/s. This phase is strongest in the secondary microcosmic band (0.1-1 Hz) but is also weakly present at longer periods (Figure 2b,c). Whereas the origin of this phase could not be conclusively ascertained, it likely arises from the interference of multiple body wave phases (see Phạm et al., 2018).

The fundamental mode Rayleigh waves group velocity dispersion curve was measured with the Multiple Filter Technique (MFT) (Dziewonski et al., 1969; Herrmann, 1973; Levshin et al., 1989). A series of narrow bandpass Gaussian filters centered at different frequencies ranging from 0.025 to 1 Hz was applied to the Rayleigh waves extracted from noise field. The arrival-time estimated from the maximum of the wave envelope for each central frequency is used together with inter-station distance to derive the group velocities for respective frequencies. Dispersion curve measurements were discarded for periods for which the inter-station distance is less than three times the wave length (Bensen et al., 2007). At this distance, the presumed fast body wave interference phase mentioned above is also well separated from the fundamental mode surface waves. Data coverage for periods from 6 to 30 s is shown in Figure 3 with the maximum number of 2326 data points (group velocity dispersion picks) obtained at a period of 9 s.

Path-average group velocities across the Ethiopian rift are shown in map view in Figure 4 for all station pairs as a function of period. Except for some extreme fast or slow velocities, in general consistent and smooth velocity variations are observed for each period.

2.2. Group Velocity Inversion

The transdimensional hierarchical Bayesian ambient noise tomography (Bodin and Sambridge, (2009) and Bodin et al. (2012a)) was developed in order to remove the influence of arbitrary choices about model parameterization and regularization. The transdimensional nature of the method means that the dimension of the model space (number of cells) is treated as unknown and allowed to vary throughout the course of the inversion in a data-driven process (Bodin et al., 2012; Young et al., 2013). The hierarchical nature of the algorithm treats the level of noise in the data set as an unknown parameter in the inversion and let the data infer its own level of uncertainty without imposing any fixed arbitrary value (Bodin et al., 2012; Dettmer et al., 2015; Galetti et al., 2016).

We applied this method to the inversion of group velocity measurements for periods between 6 and 30 s. The two-dimensional model space is partitioned into a variable number of Voronoi cells. The number, position and shape of the Voronoi cells are estimated from the data; thus the uneven spatial distribution of information is taken into account in a natural way (Young et al., 2013). In transdimensional tomography, the final model is the average of a large ensemble of independent and uniquely parametrized models that are distributed according to the posterior probability distribution (Young et al., 2013). In the implementation used here (described by Tilmann et al., 2020), the Voronoi cells are mapped onto a finer computational grid with a grid spacing of 20 km and straight ray paths are assumed.

The posterior distribution of model parameters, $P(\boldsymbol{m}|\boldsymbol{d}_{obs})$ for a given observed data, $\boldsymbol{d}_{obs}$, (travel-times) and the prior information $P(\boldsymbol{m})$ is quantified by Bayes' rule.

$$P(\boldsymbol{m}|\boldsymbol{d}_{obs}) = \frac{P(\boldsymbol{d}_{obs}|\boldsymbol{m})P(\boldsymbol{m})}{P(\boldsymbol{d}_{obs})} \qquad\qquad 1$$

where here the model $\boldsymbol{m}$ include not only the medium group slowness (inverse of group velocity) for each cell but also the number of cells and coordinates of nodes defining them, and also the parameters of the data error distribution. The term $P(\boldsymbol{d}_{obs})$, also referred to as marginal likelihood, is a normalizing constant of the posterior

distribution, which is usually difficult to calculate explicitly but is not needed for model comparison (Sambridge et al., 2006; Ray and Key, 2012).

We impose a non-informative prior distribution. The uniform prior distribution on the number of Voronoi cells is bounded between 1 and 500. The prior distribution for group slowness is also uniform, with bounds corresponding to group velocities of 0.3 km/s and 6 km/s. The lower and upper limits are chosen so generously wide such that they have negligible impact on the estimated model.

The likelihood function $P(\boldsymbol{d_{obs}}|\boldsymbol{m})$, is the probability of reproducing the observed data given the model $\boldsymbol{m}$ (Dettmer et al., 2010, 2014). In addition to the forward model, it depends on the assumed distribution of data errors. As the measurements appear to be mostly well behaved, but contain a small number of more extreme values, we assume a mixture model (following Tilmann et al., 2020), with a dominant contribution of uncorrelated and invariant Gaussian-distributed measurement errors and a minor contribution of outlier measurements modelled by a uniform distribution. This distribution gives rise to two nuisance parameters, the standard deviation σ and the relative weight of the constituent distributions. Both parameters are adjusted in a data-driven manner and form part of the posterior model distribution.

The reversible jump Markov chain Monte Carlo (RJ-MCMC) sampling algorithm (Green, 1995) is used to sample the posterior probability distribution $P(\boldsymbol{m}|\boldsymbol{d_{obs}})$. This method iteratively samples from the target distribution in a chain where each model in the chain represents a perturbation of the previous one, and new models are accepted or rejected based on $P(\boldsymbol{d_{obs}}|\boldsymbol{m})$ and $P(\boldsymbol{m})$. Generally, the Markov chain is separated into a burn-in phase, which moves the model to a part of the model space with high posterior probability, and an exploration phase, which is used to reconstruct $P(\boldsymbol{m}|\boldsymbol{d_{obs}})$ by moving the model around the high probability region. Due to the presence of complex local minima, the convergence of a single chain generally takes an unreasonably long time and is hard to ascertain in any case. Therefore, many chains are run in parallel, and combined for an estimate of the final distribution (e.g., Bodin and Sambridge, 2009). A more detailed description of the method is found in Bodin and Sambridge (2009), Dettmer et al. (2010, 2015) and Bodin et al.(2012).

Here, we consider the average and standard deviation of $P(\boldsymbol{m}|\boldsymbol{d_{obs}})$ for further processing. The final average model was produced using an ensemble of 64,000 models. A total of 2,000,000 steps were run for 64 independent Markov chains for every period between 6 and 30 s, with the first 1,000,000 discarded as burn-in. Every $1000th$ model of the post burn-in step is used to form the final average model; this sub-sampling saves memory and computational effort; due to the interdependence of nearby samples in the Markov chain, the sub-sampling only has a minor effect on the recovered distribution, as we ascertained with some exploratory tests. Figure 5 shows the progression of the Markov chains and the data fit achieved.

The average group velocity and corresponding model standard deviation are shown in Figure 6 and Figure 7, respectively. Poorly recovered areas where the standard deviation exceeds 0. 2 km/s have been trimmed. Synthetic resolution tests were performed to evaluate the reliability of the tomographic inversion and resolving power of the data. We tested two different sparse checkerboards with checker sizes (60 km and 80 km) to assess the sensitivity of our inversion for structures of different scales (Figure 8). Synthetic travel-times were computed according to the actual paths at each period and then noise with a distribution similar to the observed one was

added. In practice, the residuals of the data inversion were permuted randomly and then added to the data, such that any non-Gaussian contribution to the data noise are properly represented. We prefer the use of sparse checkerboards as test models, as they allow a better visual assessment of smearing effects. Checkerboard resolution results for periods 6, 16 and 30 s are shown in Figure 8. In general, the pattern of positive and negative anomalies is recovered well for both sizes in the region with station coverage. Only in selected areas with high station density, the neutral gaps with zero anomaly are clearly recovered.

2.3.   Shear Wave Velocity Modeling

The final step involves the inversion of the group velocity dispersion for shear wave velocity as a function of depth. To this end, the group velocities and their standard deviations were extracted from the group velocity and group velocity standard deviation maps for each node of a 0.25°x0.25° grid. The extracted dispersion curves were inverted for 1-D shear velocity structures with an iterative linearized least-square inversion scheme of Herrmann and Ammon, (2002). The 1-Dmodels were parameterized with 27 layers from the surface down to maximum depth of 50 km (Figure 9). The first ten layers are 1 km thick, layers from 10 km to 34 km are 2 km thick and from 34 km to 50 km the layer thickness becomes 4 km. Our model is not resolved below 50 km depth, and we assume a uniform velocity below 50 km depth. The P-wave velocity and density are calculated from Vs with the empirical formulas reported by Brocher (2005).

Following Ryberg et al. (2016), we base the starting model for the inversion at each grid node on a regional reference model. First, we derive an average dispersion curve of the study area by averaging all non-masked pixels of the group velocity maps at every period between 6 and 30 s (Figure 9a). The average dispersion curve was then inverted for the reference 1-D shear velocity structure using an initial model derived by referring to recent studies (Dugda et al., 2005; Stuart et al., 2006; Keranen et al., 2009; Kim et al., 2012) (Figure 9b).

The final model of this step was then used as starting model for the inversion of individual dispersion curve at each node (Figure 9b). The 3-D shear wave velocity model was then simply obtained by assembling the inverted 1-D Vs models for all nodes.

3.   Results

3.1.   Group Velocity Maps

Afar shows significant velocity heterogeneities at shallow depth as imaged by the 6 s group velocity map (between 2.4 and 2.9 km/s) and less variability at longer periods (e.g., between 3.2 and 3.4 km/s at 24 s) (Figure 6). At about 10°N an almost east-west trending high velocity zone is imaged at short periods (6 s), which marks the transition between the NMER and Afar rift. The crust beneath the MER is marked by low velocity anomalies at all periods considered, but the low velocities are very focused and clearly elongated along the rift axis for short periods and cover a wider area with a less well-defined geometry a longer period. Additionally, a linear ENE low velocity belt is observed in the southwestern plateau at 6 s periods. A NW linear low velocity belt is also imaged in the northwestern plateau at periods 10-14 s at 16 s periods. The eastern margin of the rift is generally characterized

by high velocities at intermediate periods (~16 s), with the exception of the Galema range (Sagatu volcanic line), specifically at 7°- 8° N and 39°E, where low velocities are observed.

3.2. Shear wave velocity Model

Representative 1-D shear velocity models for the different regions are shown in Figure 9b. The highest shear velocities (4.0-4.3 km/s) are generally observed in Afar in the lower crust and uppermost mantle (20-40 km). On the other hand, the MER registers the lowest shear wave velocities (3.1-3.3 km/s) in the mid-crust (12-17 km). The 1-D results obtained are in good agreement with those reported in previous studies (Dugda et al., 2005; Daly et al., 2008; Keranen et al., 2009; Kim et al., 2012; Chambers et al., 2019). Lithospheric mantle beneath the northwest plateau is imaged at a depth below 40 km and with a velocity of 4.3 km/s. The mantle below the MER has a velocity around 4.2 km/s, the lower crust has velocities 3.7-3.9 km/s, and the upper crust has 3.3-3.6 km/s. The sediments and volcanics are both characterized by a strong gradient, with velocity increasing from 2.5 to 3.3 km/s in the top 5-8 km. These values are similar to those observed by Keranen et al., (2009).

Figure 10 shows depth slices of the 3-D absolute shear velocity model. Low velocities are mapped in the Afar (3.3 km/s) and MER (3.1 km/s) at a depth of 5 km. Higher velocities (3.4-3.6 km/s) are observed in the western and eastern plateau.

At 10-20 km depth, high velocities are observed in northern Afar (including Erta' Ale). In the depth range of 20-30 km the entire Afar, with the exception of its eastern edge, is characterized by high velocities. In contrast, the entire western plateau and MER show low velocities. The most prominent anomaly at 38 km depth is the strong negative anomaly (G in Figure 10f) to the west of the Erta' Ale segment and the strong positive anomaly (H in Figure 10f) at the southern edge of the Afar.

3.3. Moho Depth

Shear wave velocity derived from surface wave inversion is not an ideal tool to map strong velocity discontinuities such as the Moho. Surface wave inversion is sensitive to crustal structure but tends to smear over discontinuities (Acton et al., 2010). Acton et al. (2010) suggest, therefore, to estimate Moho depth from surface wave models by retrieving the average velocity of the lowermost crust and uppermost mantle and taking the contour of this velocity as proxy for the Moho. Joint receiver function and surface wave study (Keranen et al., 2009) report 3.75 km/s lowermost crustal velocity and 4.1 km/s uppermost mantle velocity. The Moho depth is therefore approximately traced using the Vs=3.92 km/s contour line (Figure 11 and Figure 12). The resulting Moho undulations are in good agreement with previous studies based on receiver function analysis (Dugda et al., 2005; Stuart et al., 2006), controlled source seismic experiments (Makris and Ginzburg, 1987; Mackenzie et al., 2005; Maguire et al., 2006; Keranen et al., 2009) and 3D gravity inversion (Mammo, 2013), validating this approach and choice of velocity contour, although it has to be acknowledged that this proxy will not always reflect the Moho depth exactly, and in particular small-scale undulations of ~2-4 km should not be interpreted.

Profile I-I′ shows the structure along the rift axis from SMER to central Afar (Figure 11). The crustal thickness changes sharply from 40 km depth below the CMER to 30 km in the NMER and Afar segments, with a gradual

thinning to 26 km within the Afar. These results are in good agreement with those determined by receiver functions (Dugda et al., 2005; Stuart et al., 2006) and controlled source experiment (Mackenzie et al., 2005; Maguire et al., 2006; Keranen and Klemperer, 2008).

Profile II-II' runs parallel to the rift axis but offset by 150 km from the western plateau into the Afar. Crustal thickness varies between 34 and 44 km below the western plateau. The transition from there into the Afar is accompanied by an abrupt rise of the Moho to ~26 km and then a more gradual thinning of the crust to as low as 20 km, i.e., less than along the rift axis (Figure 11).

Profile III-III' runs perpendicular to the rift from the western plateau through the CMER onto the eastern plateau (Figure 11). The crust thins from around 40 km below the CMER to less than 32 km on the western plateau. On this cross-section the maximum depth to the Moho in the Eastern Plateau is also approximately 40 km. Such asymmetric crustal thickness with respect to the Western and Eastern Plateau was also reported in previous studies (Maguire et al., 2006; Stuart et al., 2006; Chambers et al., 2019).

4. Discussion

4.1. Upper Mantle Shear Wave Velocity Structure

The upper most mantle shear wave velocity in the study area ranges between 3.9 and 4.3 km/s, i.e., 5 – 15% lower than the upper mantle velocity of 4.5 km/s in the PREM model (Figure 9 and Figure 11). Earlier receiver function, ambient noise and surface wave studies (Dugda et al., 2007; Chambers et al., 2019; Keranen et al., 2009) reported similarly low upper mantle velocities between 3.6 and 4.3 km/s.

Possible causes of upper mantle shear wave velocity variations are mineral composition, grain size, fluid content (melt) and temperature. Compositional variations in the upper mantle cause variation of shear wave velocity by approximately 1% (Jackson et al., 2014), which is not enough to explain the observed low velocities in our region. Grain size variation from 1 mm to 10 mm at elevated temperatures can explain up to 3 % shear velocity variation (Faul and Jackson, 2005), which by itself is again insufficient to explain the observed 5 to 15 % reduction. We applied Faul and Jackson's model to relate shear wave velocity and upper mantle temperature and inferred a temperature of ~1150℃ for Vs=4.3 km/s and 1450℃ for Vs=3.8 km/s. However, a temperature of 1450℃ implies the presence of melt, which must be taken into account when converting velocity to temperature and thus would imply a somewhat lower temperature for these velocities.

4.2. Crustal Structure of the Main Ethiopian Rift

The entire crust beneath the MER south of 9.5°N is generally underlain by low velocities (Figure 10). The MER is dominated by two velocity belts, the WFB along the rift axis (A in Figure 10c) and the SDFZ on the western side of CMER (B in Figure 10c). At 5 km depth, both SDFZ and WFB are characterized by a NE-SW striking single low velocity belt (3.0-3.2 km/s, Figure 10a). At 14 km depth, the two rifts become disconnected along the Boru-Toru Structural High (BTSH) at 8.5°N, 39°E (C in Figure 10c) and start following their different courses, with the WFB propagating along the rift axis and SFDZ taking the SW trend along the Guraghe border fault.

The BTSH is an important structural feature of the MER, whose influence is not yet fully understood. However, Bonini et al. (2005) affirm that the BTSH connects the western with the eastern plateau margin near Chilalo Mountain and also serves as transfer zone separating the two different structural and tectonic domains – the NMER and CMER rift segments. A decrease in crustal thickness is seen from the CMER (~40 km) to the NMER (~33 km) immediately across the BTSH (profile I-I' in Figure 11 and Figure 13).

At mid-crustal depths (14 km) the BTSH is an almost NS trending moderately fast anomaly (Figure 10c), quickly giving way to a slow anomaly at its southern end where it meets the rift axis of the CMER. This sudden reversal in velocity perturbation at the rift axis could be interpreted as the result of activity and extensional deformation expressed as concentration of partial melts and dike intrusions as well as caldera formation in the Gedemsa (G) and Tullu Moye (T) volcanic centers (Figure 13).

This result appears to favor the model given by Rooney et al., (2007) (Figure 13a) over the models suggested by Wolfenden et al., (2004) to account for the propagation of extensional deformation in the Main Ethiopian Rift. The model of Rooney et al., (2007) considers the MER as a place where two rifts join - the WFB representing the southward extension of the Red Sea Rift and the SDFZ representing the northward propagation of EARS, with the WFB eventually breaching the BTSH and interacting with SDFZ in CMER (Figure 13b). They also noted that the two rifts are characterized by different magmatic systems and magmatic activities.

Previous studies show that rifting started along the border faults and progressively migrated towards the center where deformation is accommodated by magmatic activity and dike intrusion in the rift floor (Bilham et al., 1999; Ebinger and Casey, 2001; Wolfenden et al., 2004). However, a wide zone of low velocities imaged at shallow depth (5 km) below both the MER and Afar is not confined to the rift center but extends beyond, indicating that tectonic and magmatic activities in the MER and Afar are widespread within the upper crust. This observation is also consistent with the GPS data, which indicate that strain is distributed over wide areas in both Afar and the MER (Kogan et al., 2012).

The cross-section along the rift axis from the southern MER to southern Afar (profile I-I') (Figure 11) shows a 40 km thick crust beneath the CMER. Keranen and Klemperer (2008) and Corti (2009) interpreted this crust as less magmatically modified and less extended in comparison with that of NMER. However, at upper crustal depth (5-10 km) the CMER is dominated by very low shear wave velocities, particularly adjacent to the western margin alongside the SDFZ (Figure 10a). These results are consistent with the high Vp/Vs ratios (>2) in receiver function studies, which were interpreted as evidence for the presence of partial melt within the crust (Stuart et al., 2006). Geochemical analysis has also revealed evidence for magma in the crust under the SDFZ (Rooney et al., 2005, 2007). The plumbing model proposed by Rooney et al. (2005) suggested fractionation to have taken place throughout the crust. An earlier ambient noise tomography study also indicated that the crust beneath the SDFZ has been substantially modified by mafic intrusions (Kim et al., 2012).

4.3.   Crustal Structure of the Afar Depression

The upper crust beneath Afar is characterized by shear wave velocities in between 3.1 and 3.6 km/s (Figure 10). At 5 km depth low shear velocities (3.2-3.3 km/s) span most of the region underlying Afar. The low velocity in

central Afar (D in Figure 10a) is correlated with the surface exposure of Pliocene flood basalts. The decrease in wave speed is interpreted as the effect of elevated temperature and partial melt in the upper crust, which is also evident from the surface expression of volcanism and thermal activity.

At 14 km depth, low shear velocities (~3.3 km/s) are observed around the Alayta and Dabbahu magmatic segments (E in Figure 10c). Between 2005 and 2010 these regions have experienced over 14 large dike intrusions (Ebinger et al., 2010; Ferguson et al., 2013). Seismicity, the structural pattern and modeling of InSAR data indicate that the September – October 2005 earthquakes were accompanied by emplacement of a 60 km-long basaltic dike intrusion along the Dabbahu segment with a maximum opening of 8 m (Wright et al., 2006; Yirgu et al., 2006; Ayele et al., 2007; Keir et al., 2009).

A high velocity perturbation appears beneath Erta' Ale at depths greater than 14-20 km (>3.7 km/s), extending to the southeast parallel to the Red Sea Rift (F in Figure 10d). This high velocity perturbation extends from Erta' Ale to the Alayta-Dabbahu-Manda Hararo magmatic segments where incipient ocean floor is developing. This suggests that rifting at Erta' Ale is at an earlier stage and becomes successively younger southward along the magmatic segments. This interpretation is consistent with the conclusion by Bastow and Keir, (2011) that Erta' Ale is at a more advanced stage of rifting than Central Afar.

A prominent feature in the deepest part of our model (~38 km) is the very slow (Vs ~3.7 km/s) arcuate structure at the western Afar margin at 14°N, which extends towards central Afar (G in Figure 10f). This anomaly could indicate an earlier rift axis in northern Afar, possibly extending further north into the Gulf of Zula through the Alid graben (around 14.8°N and 39.9°E). This abandoned rift was superseded by a more active rift at its southern end, along the current axial range. It has been argued that the expansion of the latter rift was facilitated by the anticlockwise rotation of the Danakil microplate and clockwise rotation of the Ali Sabieh block (Souriot and Brun, 1992; Eagles et al., 2002; Audin et al., 2004).

Relatively high velocities, compared to the rest of the study region, (up to 4.4 km/s) are imaged in southeastern Afar at a depth of 40 km in the upper mantle (H in Figure 10e). This anomaly is bounded in the east by the Ali-Sabeh block, in the west by the WFB and in the south by the eastern plateau. This place was earlier occupied by the Ali-Sabeh microplate before it was torn from the eastern plateau and rotated 90° clockwise to its present position (Manighetti et al., 2001; Beyene and Abdelsalam, 2005). The velocity anomaly probably arises due to the fast mafic materials associated with the separation of the microplate.

To summarize, the observed low velocities (< 3.4 km/s) prevalent in the upper crust (<14 km) suggest that the crust in the whole Afar is highly stretched with pervasive partial melts and that it is thus on the verge of transitioning to oceanic spreading.

4.4. Western Plateau

Immediately after the eruption of the trap basalts huge shield volcanoes developed on the plateau. Among these is the 4190 m high Mt. Abune Yosef (J in Figure 10a), situated at the rift shoulder. Beneath this volcano, an almost circular low velocity anomaly is imaged at 5 km depth (J in Figure 10a). North of 12.5°N, the Precambrian

basement including the Mekelle outlier (limestone) is characterized by high velocities in the upper crust (Figure 10a). At 10 km depth, however, the central part of the western plateau is instead characterized by a prominent low velocity anomaly (3.2-3.3 km/s) beneath the shield volcanoes Guguftu, Choke and Guna, which penetrates the whole crust (with varying strength) down to at least 40 km depth (K in Figure 10). The low velocities imply that the western plateau is magmatically active.

A localized low shear velocity (3.2 km/s) is imaged between the Alayta magmatic segment and the western flank of the rift around 10 km depth (L in Figure 10b). In addition, a low velocity perturbation is observed beneath the Ankober border fault (M in Figure 10d). This suggests that magmatism on the flank is still active, leading to a concentration of partial melts in reservoirs or dike intrusions. Similarly low velocities also arise in the ambient noise tomography of Korostelev et al., 2015). In addition, the frequent earthquakes occurring along the border faults (Asfaw, 1992; Keir et al., 2006) confirm that the border faults are still active.

Therefore, the border faults and the rift axes both shape the tectonic evolution of rifting in the MER and in Afar. The kinematic model of Muluneh et al. (2014) and Muluneh et al. (2018) relates the orientation of the rift to the relative motions of the Nubian and Somalian plates in Hotspot Reference Frame.

4.5. The Off Axis Low Velocity Belts

Low velocity belts have been imaged beneath the western and eastern plateaus away from the active rift axes. These belts might represent failed or buried rifts filled with sediments or low velocity clastic rocks. If this interpretation is correct, the traces of the old rift can be used to reconstruct the evolution of the rift system (Kearey and Vine, 2004).

4.5.1. The ENE trending low velocity belt

From the YTVL-MER junction a prominent low velocity belt (~3.2 km/s) extends southwest ward across the SW plateau between 36.5°-39°E and 7.5-9°N in the shallow crust; a ENE trending anomaly is strongest in the 5 km depth slice but it still visible at 10 km depth (O in Figure 10a). This structure probably represents an ancient rift buried beneath the volcanic series. Zanettin and Justin-Visentin, (1974, 1975), Zanettin et al., (1974, 1980), Piccirillo et al., (1979) and Zanettin, (1993) already suggested the existence of the so-called Ashangi rift at this location, based on evidence for Pre-Oligocene volcanism. Moreover, Zanettin et al., (1974) also suggested that due to the slow but continuous uplift of its western margin, the rift progressively shifted towards the east, each abandoned rift being replaced by a younger one to the east until the current rift formed. If this proves to be correct then there is a possibility that it could serve as an alternative model to account for the formation and development of the MER.

Until now no evidence has been able to confirm the existence of the buried Ashangi rift. The low velocity belt in our model may be the fossil trace of the Ashangi rift.

4.5.2. The NNE trending low velocity belt

The NNE trending off axis ~80 km long and 7 km wide km Galema range (Segatu) is situated at 39.4°E and 7°-8°N in the eastern shoulder of the MER, where it is superimposed on the eastern plateau (P in Figure 10c,f). The range is about 80 km away from WFB and 40 km east of the Asela-Sire Border fault and its Pliocene age fissure system represents an area of focused magmatic activity, with its core comprising complex dike swarms, lavas and cinder cones (Mohr and Potter, 1976; Mohr et al., 1980; Woldegabriel et al., 1990; Chiasera et al., 2018). Its evolution is probably controlled by pre-existing structural weakness (Corti et al., 2018).

The shear velocity model indicates the presence of a low velocity anomaly at depths of 10 to 18 km and at deeper depths of 32 to 38 km with intermediate velocities in between (P in Figure 10c,f). Chiasera et al., (2018) used whole-rock thermodynamic modeling and thermobarometric calculations on mineral-liquid pairs to infer two fractionation depths. The presence of two distinct magmatic reservoirs provides a natural explanation for the two zones of very low velocities mentioned above.

5. Conclusions

We presented new Rayleigh wave group velocity maps of the crust and uppermost mantle over most of the tectono-magmatically active parts of Ethiopia using hierarchical Bayesian ambient seismic noise tomography. A shear wave velocity model of the crust was then produced for the entire region based on the point-wise linearized inversion of the dispersion curves extracted from the group velocity maps. The shear velocities inferred for the study region range between 2.6 – 4.3 km/s. Both crust and mantle are characterized by unusually low velocities, up to 15% less than the PREM model in the uppermost mantle. The combined effect of temperature and melt is needed to explain such a large shear wave velocity reduction. Although surface wave inversion has low sensitivity to discontinuities, we obtained a coarse estimate of the Moho depth from the 3.92 km/s contour. The maximum Moho depth in the study region is found beneath the western plateau. The Moho is imaged at a depth of ~38 km in the CMER, at 31-33 km in the NMER and at <20 km in northern Afar.

The main findings extracted from our velocity model are: (1) Off-axis low shear wave velocity belts are imaged beneath both the eastern and western plateaus, which are interpreted to be failed or buried rifts. (2) The rift flanks and border faults are still active both tectonically and magmatically. (3) Tectonic and magmatic activities are not localized to the rift center, but widespread in the upper crust within both the MER and Afar. (4) The MER is dominated by two velocity belts, the WFB along the rift axis and the SDFZ on the western side of the CMER; the BTSH appears to serve as a transfer zone between them. (5) The crust beneath the western plateau is characterized by a low velocity anomaly, implying that the plateau is also tectonically and magmatically active.
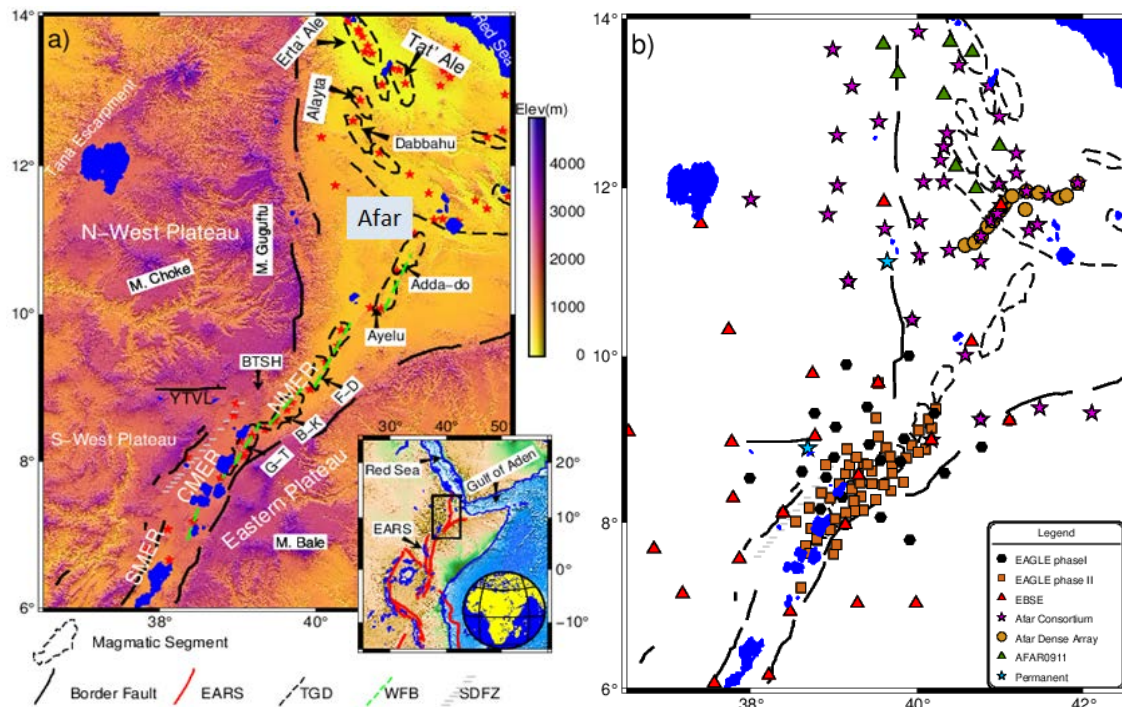
Acknowledgements

Figure 1 *a) Topographic map of the Ethiopian rift and adjacent plateaus. Major quaternary volcano centers are shown by the red asterisk and lakes and ocean are indicated by the blue polygons. CMER: central main Ethiopian rift; NMER: northern main Ethiopian rift; SMER: southern main Ethiopian rift; G-T: Gedemsa-Tullu Moye magmatic segment; B-K: Boset-Kone magmatic segment; F-D: Fentale-Dofan magmatic segment; SDFZ: Silti-Debre Zeit Fault Zone; TGD: Tendaho-Goba'ad discontinuity; YTVL: Yerer Tullu Welel Volcano Tectonic Lineaments; BTSH: Boru-Toru Structural High; WFB: Wonji Fault Belt; EARS: East African Rift System. The inset shows the wider context of the study area. b) Distribution of seismic stations.*
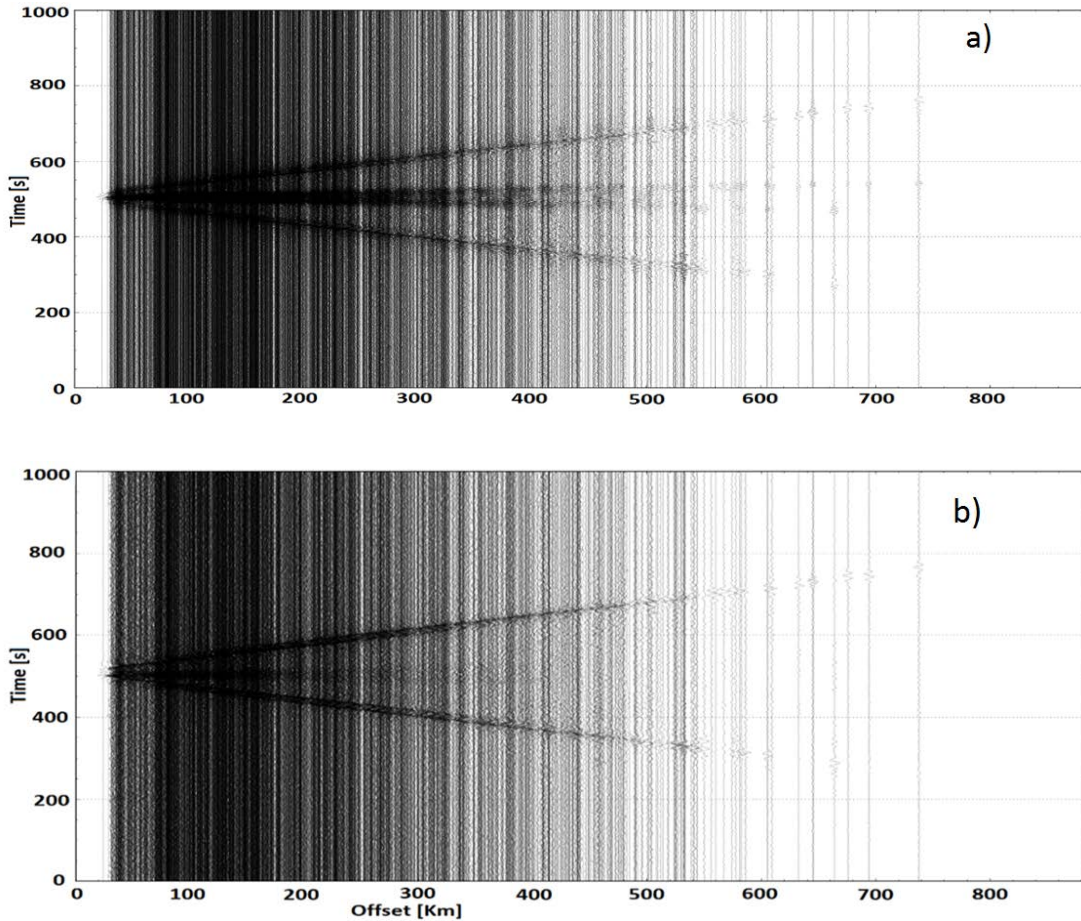
Figure 2 *Vertical component Empirical Green's functions for all station pairs with good signal to noise ratio, sorted as a function of interstation distance. (a) The time series have been filtered between 0.1 and 0.025 Hz. The dominant signal is corresponding to Rayleigh waves of velocity 3.3 - 3.5 km/s. (b) The same as (a), but bandpass filtered between 0.4 and 0.1 Hz. Apart from the dominant signal of the presumed surface wave, there is a clearly identifiable signal with much smaller move-out, traveling with ~20 km/s (see text for discussion).*
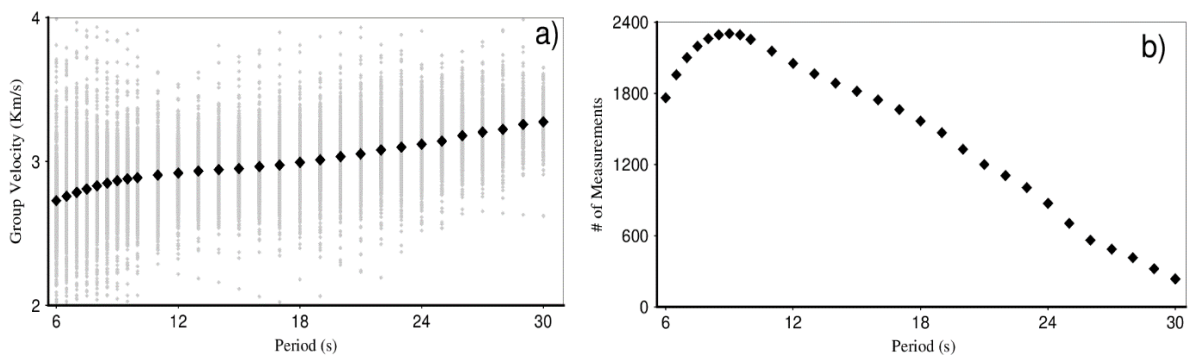
Figure 3 *Group velocity extracted from cross correlation functions. a) Gray dots show individual dispersion points. Black dots indicate average dispersion curve. b) Total number of group velocity measurements satisfying the far field criterion and with good signal-to-noise ratio, as a function of period.*
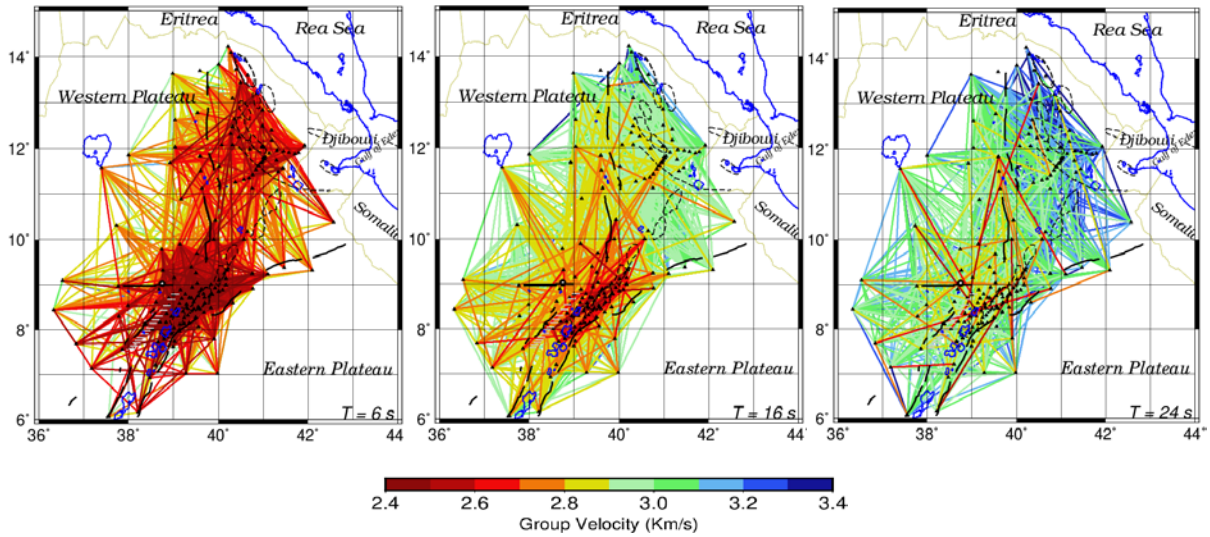
Figure 4 *Interstation group velocity measurements for periods 6, 16 and 24 s.*
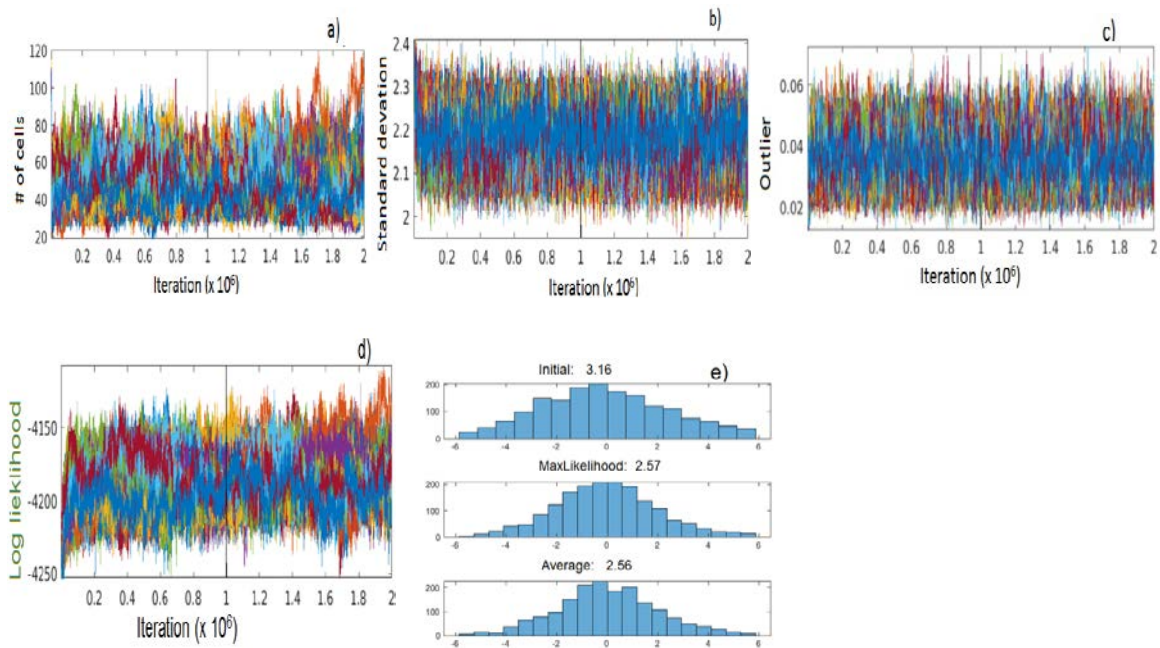

Figure 5 *Posterior distribution from transdimensional tomography at a period of 16 s, using 64 independent chains (distinguished by color). In (a) to (d), a vertical bar at 1 million iterations marks the end of the burn-in phase. (a) Number of Voronoi cells. (b) Estimated standard deviation of data uncertainty distribution. (c) Estimated outlier fraction. (d) Log likelihood. (e) Histograms of residuals with respect to uniform velocity model (top), maximum likelihood model (middle) and average model (bottom). Additionally, the corresponding residual root mean square is indicated in title of each of the three panels.*
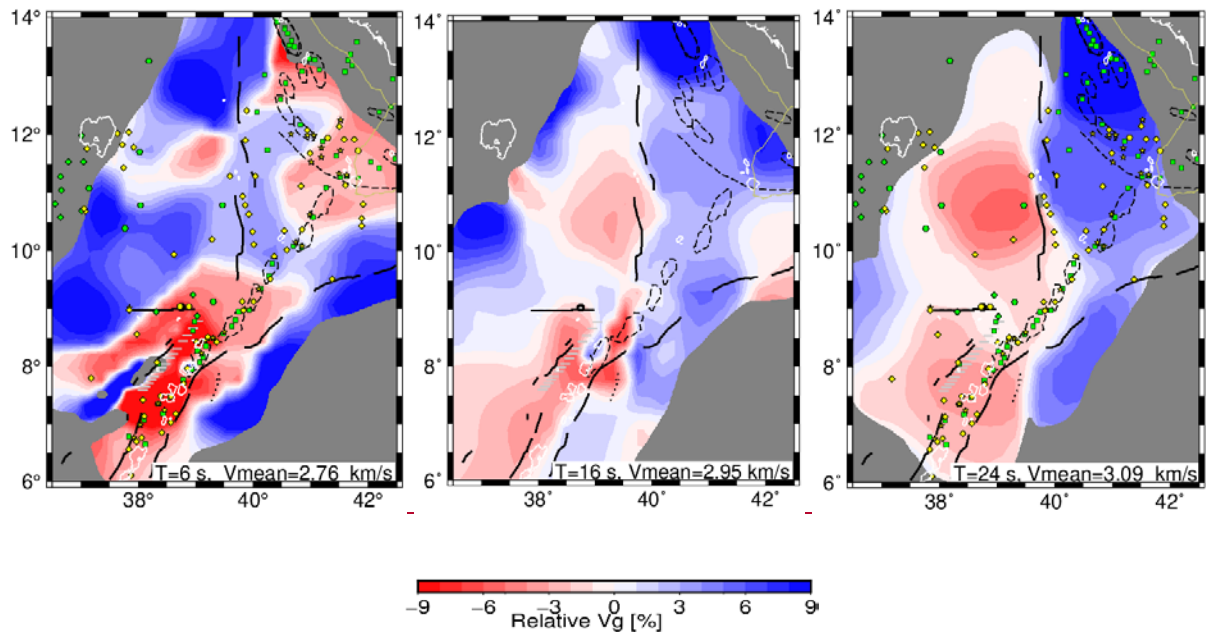
Figure 6 *Average group velocity maps for periods 6, 16 and 24 s. Group velocities are perturbations in percent relative to the mean velocity indicated on each map. Yellow diamonds, stars and hexagons show the location of thermal springs, fumaroles and thermal wells, respectively (adapted from Keir et al., (2009)). Selected volcanic centers are indicated with green squares. BTSH: Boru-Toru Structural High, ENE-LVB: East north east-trending low velocity belt.*
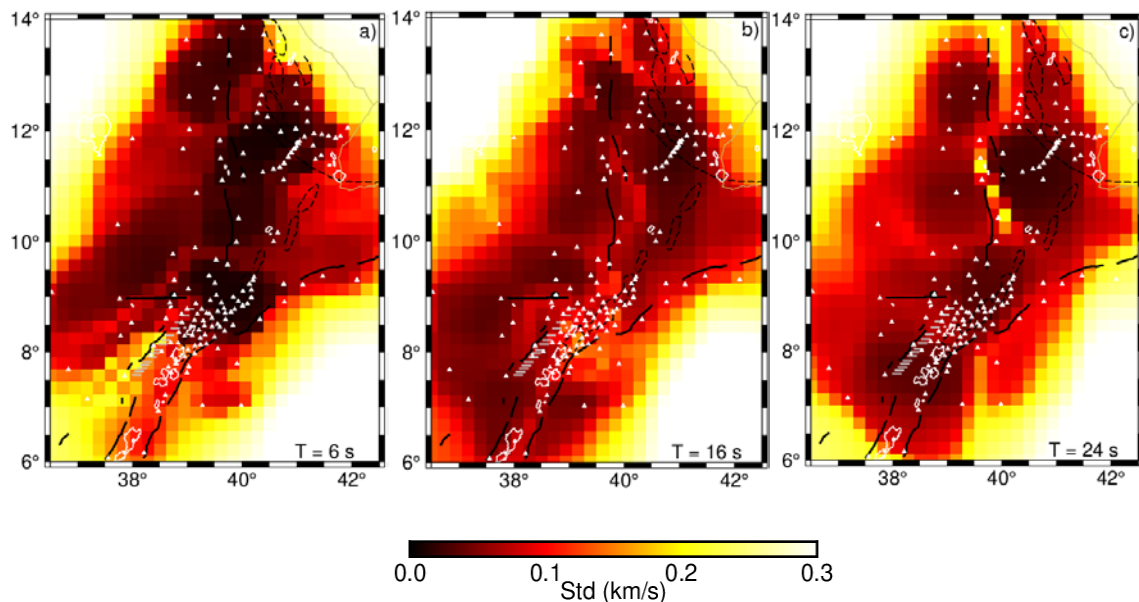

Figure 7 *Rayleigh group velocity posterior standard deviation maps (km/s) for periods 6, 16 and 24 s. Stations (white triangles), border faults and magmatic segments are the same as in Figure 1.*
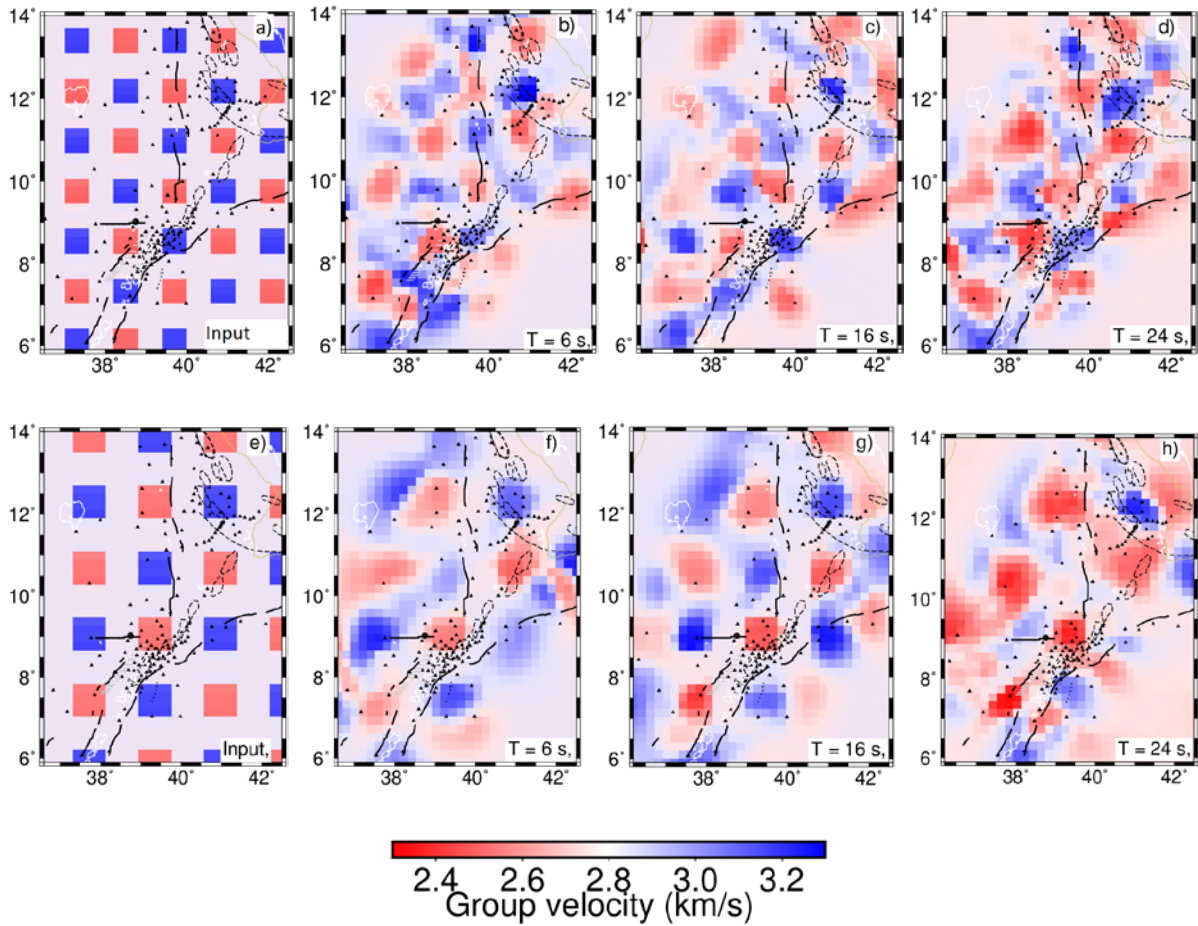
Figure 8 *Checkerboard resolution test for periods 6, 16 and 24 s. Two input models of checker size 60 km and 80 km size are used. Stations (black triangles), border faults and magmatic segments are the same as in Figure 1. Note that the grid spacing of the computational grid (see text) was set to the size of the input checkers.*
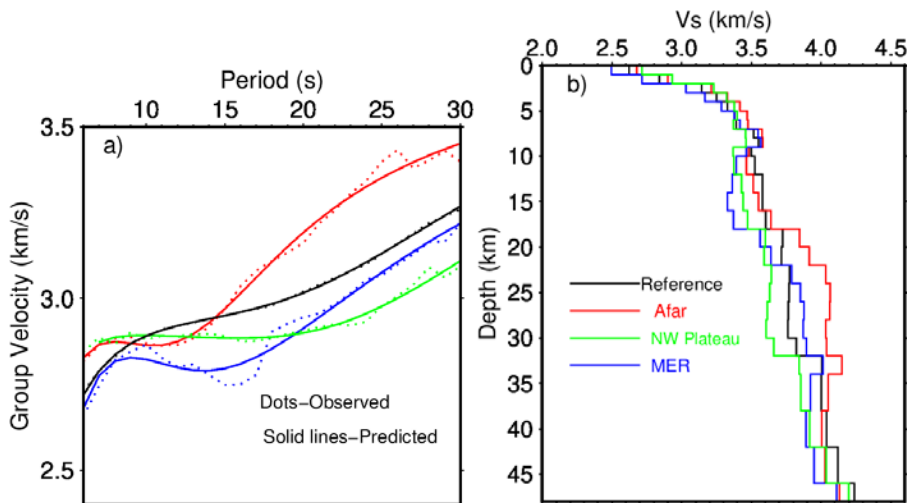

Figure 9 *(a) Observed (from group velocity tomography) and predicted dispersion curves from representative locations in various tectonic regimes (A, G and K for MER, Afar and the western plateau, respectively (see FIGURE 10b for locations). The black line represents the average dispersion curve for the study area. (b) The 1-D shear wave velocity structures corresponding to the dispersion curves shown in a.*
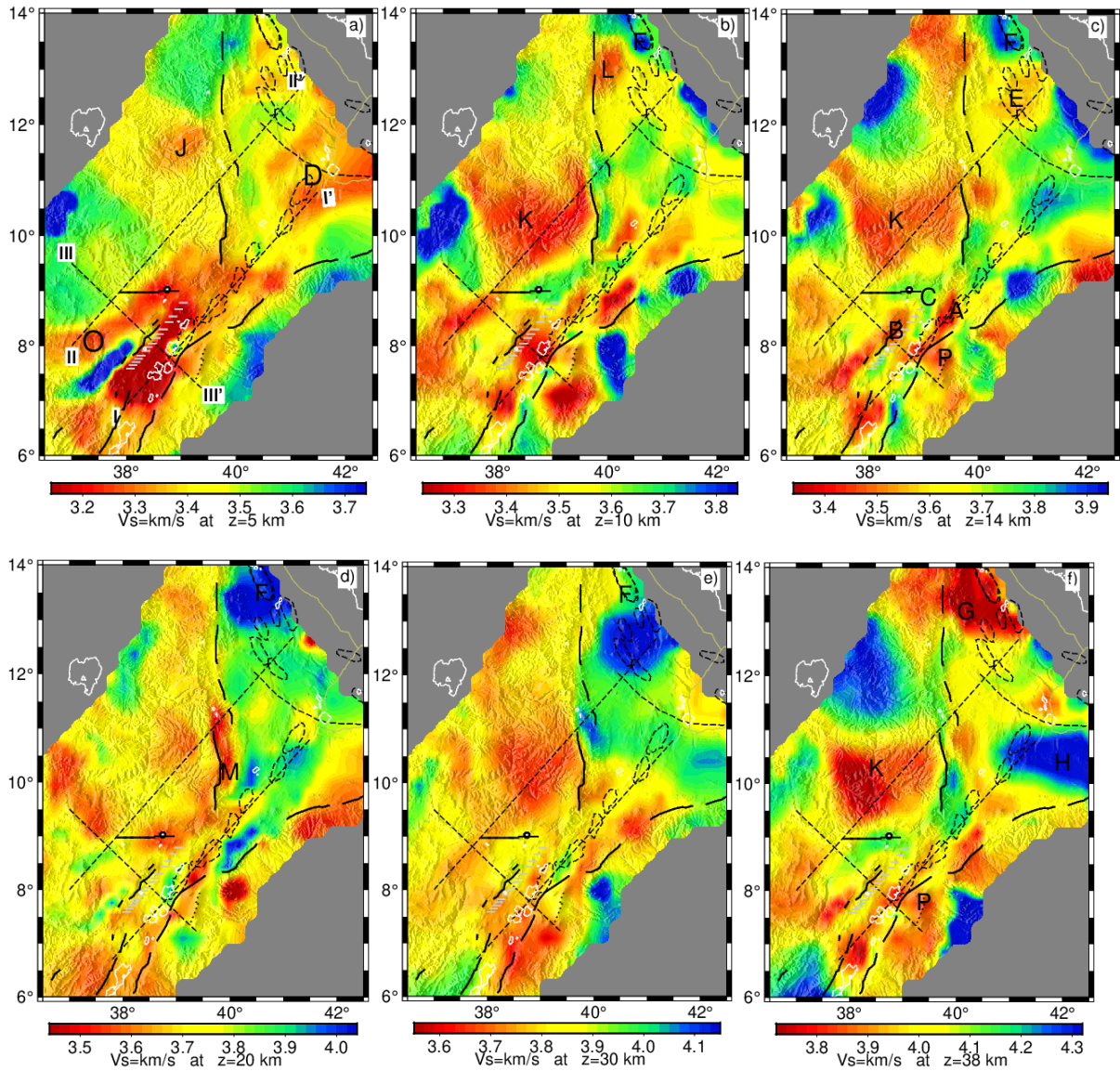
Figure 10 *Maps of shear velocity at selected depths. In (a), dotted lines are 2-D profiles along which cross sections of shear velocity structures are plotted and reported in* Figure 11. *Note that color scales have been adjusted based on the reference model velocity at each depth, but that the range of velocities covered is identical for all color scales. Black labels mark high and low velocity anomalies for use in the Discussion. As in Fig. 1, continuous black lines designate border faults, and dotted black curves show magmatic centers. Continuous white lines show shorelines of major lakes and the Red Sea. Yellow line represents political boundary.*
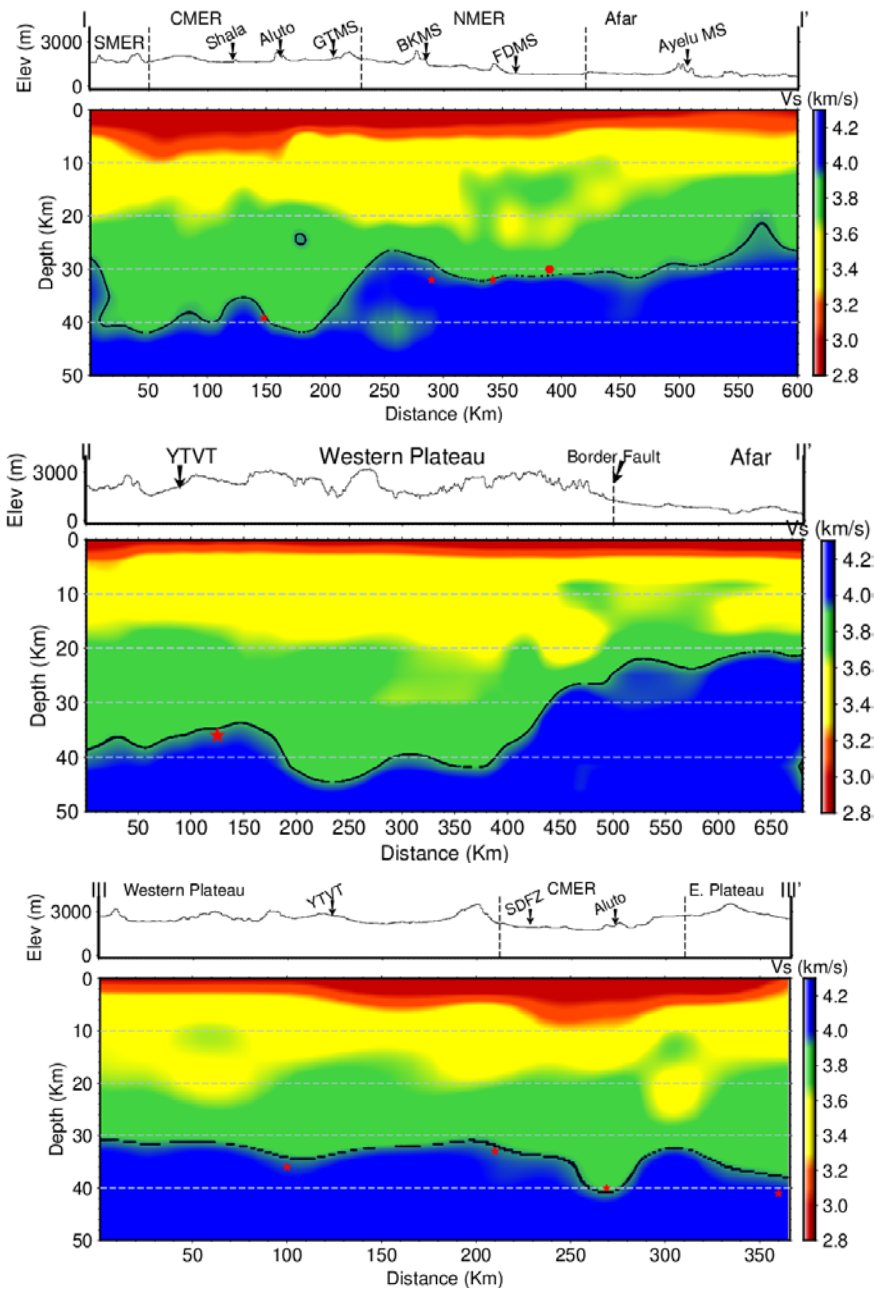
19

Figure 11 *Cross-sections through the shear velocity model. Locations of cross sections are shown in Fig. 10a. Elevation, major tectonic and geological features are indicated on top of each cross-section. Black dots express an estimate of the Moho depth based on the 3.92 km/s contour (see text). Red stars and hexagons show depth of Moho from receiver functions* (Dugda et al., 2005; Stuart et al., 2006) *and controlled source studies* (Makris and Ginzburg, 1987), *respectively.*
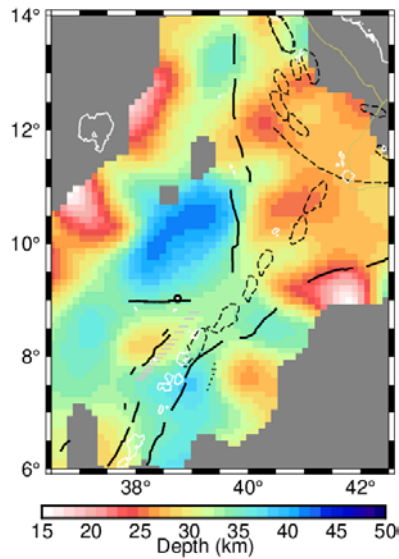
Figure 12 *Depth to Moho, estimated as 3.92 km/s contour of the final velocity model.*
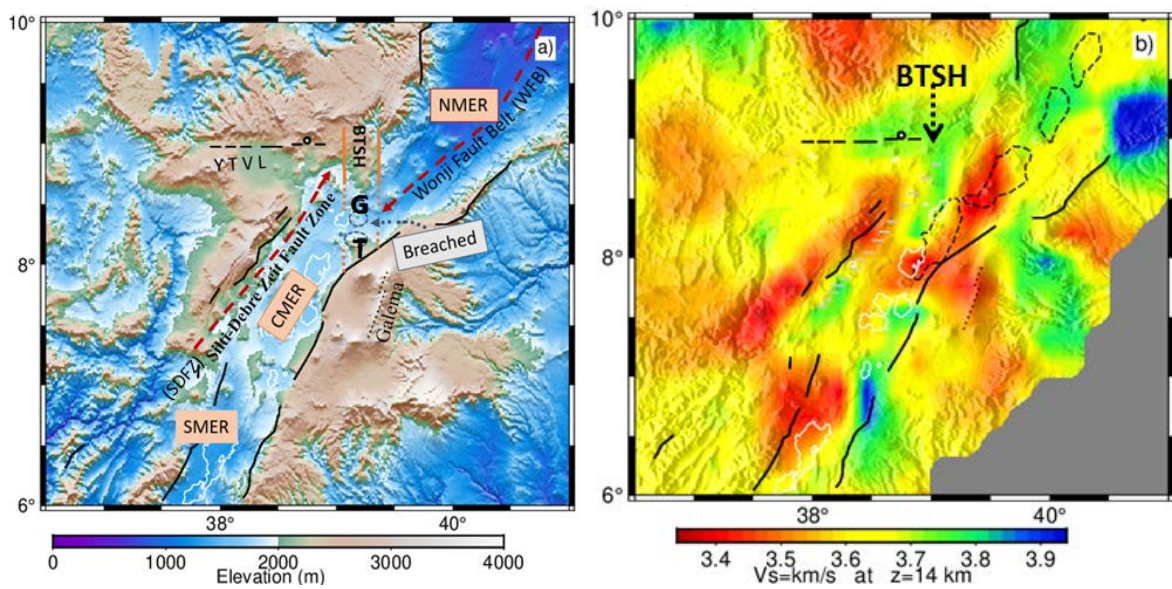

FIGURE 13 *Main Ethiopian Rift: (a) topography with the location of Boru-Toru Structural High (BTSH) highlighted, volcanic centers G: Gedemsa, T: Tullu Moye .(b) Shear wave velocity model at depth of 14 km showing a high velocity perturbation under the BTSH and low shear velocities beneath the Silti-Debre Zeit Fault zone and Wonji Fault Belt.*

References

Abbate, E., Bruni, P., and Sagri, M., 2015, Geology of Ethiopia: A Review and Geomorphological Perspectives. In: Billi P (ed) Landscapes and landforms of Ethiopia: Springer, Dordrecht, 33-64 p., doi:10.1007/978-94-017-8026-1_2.

Abebe, T., Abeba, A., Pira, V. La, Maria, V.S., and Maria, V.S., 1998, The Yerer-Tullu Wellel volcanotectonic lineament : a transtensional structure in central Ethiopia and the associated magmatic activity: Journal of African Earth Sciences, v. 26, p. 135–150.

Acocella, V., Abebe, B., Korme, T., and Barberi, F., 2008, Structure of Tendaho Graben and Manda Hararo Rift : Implications for the evolution of the southern Red Sea propagator in Central Afar: Tectonophysics, v. 27, p. TC4016, doi:10.1029/2007TC002236.

Acton, C.E., Priestley, K., Gaur, V.K., and Rai, S.S., 2010, Group velocity tomography of the Indo - Eurasian collision zone: Journal of Geophysical Research, v. 115, p. 1–16, doi:10.1029/2009JB007021.

Asfaw, L.M., 1992, Seismic risk at a site in the East African rift system: Tectonophysics, v. 209, p. 301–309.

Audin, L., Quidelleur, X., Couli, E., Courtillot, V., Gilder, S., Manighetti, I., Gillot, P., Tapponnier, P., and Kidane, T., 2004, Palaeomagnetism and K-Ar and 40 Ar / 39 Ar ages in the Ali Sabieh area (Republic of Djibouti and Ethiopia): constraints on the mechanism of Aden ridge propagation into southeastern Afar during the last 10 Myr: Geophysical Journal International, v. 158, p. 327–345, doi:10.1111/j.1365-246X.2004.02286.x.

Ayalew, D., 2011, The relations between felsic and mafic volcanic rocks in continental flood basalts of Ethiopia : implication for the thermal weakening of the crust Gondor Bahir Dar Injibara Dessie: The Geological Society of London, v. 357, p. 253–264, doi:DOI: 10.1144/SP357.13.

Ayele, A., Stuart, G., Bastow, I., and Keir, D., 2007, The August 2002 earthquake sequence in north Afar : Insights into the neotectonics of the Danakil microplate: Journal of African Earth Sciences, v. 48, p. 70–79, doi:10.1016/j.jafrearsci.2006.06.011.

Bastow, I.D., and Keir, D., 2011, The protracted development of the continent – ocean transition in Afar: Nature Geoscience, doi:10.1038/ngeo1095.

Bensen, G.D., Ritzwoller, M.H., Barmin, M.P., Levshin, A.L., Lin, F., Moschetti, M.P., Shapiro, N.M., and Yang, Y., 2007, Processing seismic ambient noise data to obtain reliable broad-band surface wave dispersion measurements: Geophysical Journal International, v. 169, p. 1239–1260, doi:10.1111/j.1365-246X.2007.03374.x.

Beyene, A., and Abdelsalam, M.G., 2005, Tectonics of the Afar Depression : A review and synthesis: Journal of African Earth Sciences, v. 41, p. 41–59, doi:10.1016/j.jafrearsci.2005.03.003.

Bilham, R., Bendick, R., Larson, K., Braun, J., Tesfaye, S., Mohr, P., and Asfaw, L., 1999, Secular and tidal strain across the Ethiopian rift: Geophysical Research Letters, v. 27, p. 2789–2984.

Bodin, T., and Sambridge, M., 2009, Seismic tomography with the reversible jump algorithm: Geophysical Journal International, v. 178, p. 1411–1436, doi:10.1111/j.1365-246X.2009.04226.x.

Bodin, T., Sambridge, M., Rawlinson, N., and Arroucau, P., 2012, Transdimensional tomography with unknown data noise: Geophysical Journal International, v. 189, p. 1536–1556, doi:10.1111/j.1365-246X.2012.05414.x.

Bonini, M., Corti, G., Innocenti, F., Manetti, P., Mazzarini, F., Abebe, T., and Pecskay, Z., 2005, Evolution of the Main Ethiopian Rift in the frame of Afar and Kenya rifts propagation: Tectonics, v. 24, p. 1–21, doi:10.1097/SLA.0000000000001986.

Brocher, T.M., 2005, Empirical Relations between Elastic Wavespeeds and Density in the Earth ' s Crust: Bulletin of the Seismological Society of America, v. 95, p. 2081–2092, doi:10.1785/0120050077.

Buck, W.R., 2006, The role of magma in the development of the Afro-Arabian Rift System. In: The Afar Volcanic Province within the East African Rift System (G. Yirgu, C.J. Ebinger and P.K.H. Maguire, eds): TGeological Society, London, Special Publications, v. 259, p. 43–54.

Campillo, M., and Paul, A., 2003, Long-Range correlations in the diffuse seismic coda: Science, v. 299, p. 547–549.

Chambers, E.L., Harmon, N., Keir, D., and Rychert, C.A., 2019, Using Ambient Noise to Image the Northern East African Rift: Journal of Geophysical Research, v. 20, p. 2091–2109, doi:10.1029/2018GC008129.

Chiasera, B., Rooney, T.O., Girard, G., Yirgu, G., Grosfils, E., Ayalew, D., Mohr, P., Zimbelman, J.R., and Ramsey, M.S., 2018, Magmatically assisted off-rift extension — The case for broadly distributed strain accommodation: Geosphere, v. 14, p. 1544–1563.

Corti, G., 2009, Earth-Science Reviews Continental rift evolution : From rift initiation to incipient break-up in the Main Ethiopian Rift , East Africa: Earth Science Reviews, v. 96, p. 1–53, doi:10.1016/j.earscirev.2009.06.005.

Corti, G., Molin, P., Sembroni, A., Bastow, I.D., and Keir, D., 2018, Control of Pre-rift Lithospheric Structure on the Architecture and Evolution of Continental Rifts: Insights From the Main Ethiopian Rift, East Africa: Tectonics, v. 37, p. 477–496, doi:10.1002/2017TC004799.

Daly, E., Keir, D., Ebinger, C.J., Stuart, G.W., Bastow, I.D., and Ayele, A., 2008, Crustal tomographic imaging of a transitional continental rift : the Ethiopian rift: Geophysical Journal International, v. 172, p. 1033–1048, doi:10.1111/j.1365-246X.2007.03682.x.

Dettmer, J., Benavente, R., Cummins, P.R., and Sambridge, M., 2014, Trans-dimensional finite-fault inversion: Geophysical Journal International, v. 199, p. 735–751, doi:10.1093/gji/ggu280.

Dettmer, J., Dosso, S.E., and Holland, C.W., 2010, Trans-dimensional geoacoustic inversion: Journal of Acoustical society of America, v. 128, p. 3393–3405, doi:10.1121/1.3500674.

Dettmer, J., Holland, C.W., and Dosso, S.E., 2015, Transdimensional uncertainty estimation for dispersive seabed sediments Transdimensional uncertainty estimation for dispersive seabed sediments: Geophysics, v. 78, p. WB63–WB76, doi:10.1190/geo2012-0358.1.

Dias, R.C., Julià, J., and Schimmel, M., 2015, Rayleigh-Wave, Group-Velocity Tomography of the Borborema Province, NE Brazil, from Ambient Seismic Noise: Pure and Applied Geophysics, v. 172, p. 1429–1449, doi:10.1007/s00024-014-0982-9.

Dugda, M.T., Nyblade, A.A., and Julia, J., 2007, Thin Lithosphere Beneath the Ethiopian Plateau Revealed by a Joint Inversion of Rayleigh Wave Group Velocities and Receiver Functions: Journal of Geophysical Research, v. 112, p. 1–14, doi:10.1029/2006JB004918.

Dugda, M.T., Nyblade, A.A., Julia, J., Langston, C.A., Ammon, C.J., and Simiyu, S., 2005, Crustal structure in Ethiopia and Kenya from receiver function analysis : Implications for rift development in eastern Africa: Journal of Geophysical Research, v. 110, p. B01303, doi:10.1029/2004JB003065.

Dziewonski, A., Bloch, A., and Landisman, M., 1969, A technique for the analysis of transient seismic signals: Bulletin of the Seismological Society of America, v. 59, p. 427 – 44.

Eagles, G., Gloaguen, R., and Ebinger, C., 2002, Kinematics of the Danakil microplate: Earth and Planetary Science Letters, v. 203, p. 607–620.

Ebinger, C., Ayele, A., Keir, D., Rowland, J., Yirgu, G., Wright, T., Belachew, M., and Hamling, I., 2010, Length and Timescales of Rift Faulting and Magma Intrusion : The Afar Rifting Cycle from 2005 to Present: Earth

and Planetary Science Letters, v. 38, p. 437–464, doi:10.1146/annurev-earth-040809-152333.

Ebinger, C., and Casey, M., 2001, Continental breakup in magmatic provinces : An Ethiopian example: Geological Society of America, v. 29, p. 527–530.

Faul, U.H., and Jackson, I., 2005, The seismological signature of temperature and grain size variations in the upper mantle: Earth and Planetary Science Letters, v. 234, p. 119–134, doi:10.1029/2001JB001225.

Ferguson, D.J., Maclennan, J., Bastow, I.D., Pyle, D.M., Jones, S.M., Keir, D., Blundy, J.D., Plank, T., and Yirgu, G., 2013, Melting during late-stage rifting in Afar is hot and deep: Nature, v. 498, p. 70–73, doi:10.1038/nature12292.

Galetti, E., Curtis, A., Baptie, B., Jenkins, D., and Nicolson, H., 2016, Transdimensional Love-wave tomography of the British Isles and shear-velocity structure of the East Irish Sea Basin from ambient-noise interferometry: Geophysical Journal International, p. 1–46.

Gao, S., 2009, Four-Dimensional Anatomy of Continental Rifts Transitioning into Sea Floor spreading: Insights from Afar, Ethiopia for oil and gas exploration of global rift systems and passive continental margins: International Federation of Digital Seismograph Networks, doi:https://doi.org/10.7914/SN/ZK_2009.

Green, P.J., 1995, Reversible jump Markov chain Monte Carlo computation and Bayesian model determination: Biometrika, v. 82, p. 711–732.

Herrmann, R.B., 1973, SOME ASPECTS OF BAND-PASS FILTERING OF SURFACE WAVES: Bulletin of the Seismological Society of America, v. 63, p. 663–671.

Herrmann, R.B., and Ammon, C.J., 2002, Computer programs in seismology: Surface waves, receiver functions and crustal structure: Saint Louis University,.

Hofmann, C., Courtillot, V., Feraud, G., Rochette, P., Yirgu, G., Ketefo, E., and Pik, R., 1997, Timing of theEthiopian floodbasalt event and implications forplume birthand global change: Letters to nature, v. 389, p. 838–841.

Jackson, I., Faul, U.H., and Skelton, R., 2014, Elastically accommodated grain-boundary sliding : New insights from experiment and modeling: Physics of the Earth and Planetary Interiors, v. 228, p. 203–210.

Kazmin, V., Berhe, S.M., Nicoletti, M., and Petrucciani, C., 1980, Evolution of the northern part of the Ethiopian rift: Rendiconti dell'Accademia Nazionale dei Lincei, Rome, v. 47, p. 275–292.

Kearey, P., and Vine, F.J., 2004, Global Tectonics, Blackwell Science:

Keir, D., Bastow, I.D., Daly, E., and Cornwell, D.G., 2009, Lower crustal earthquakes near the Ethiopian rift induced by magmatic processes: Geochemistry, Geophysics, Geosystems, v. 10, p. 1–10, doi:Q0AB02,10.1029/2009GC002382.

Keir, D., Ebinger, C.J., Stuart, G.W., Daly, E., and Ayele, A., 2006, Strain accommodation by magmatism and faulting as rifting proceeds to breakup : Seismicity of the northern Ethiopian rift: Journal of Geophysical Research, v. 111, p. 1–17, doi:10.1029/2005JB003748.

Keir, D., and Hammond, J.O.S., 2009, AFAR0911: nternational Federation of Digital Seismograph Networks, doi:https://doi.org/10.7914/SN/2H_2009.

Keranen, K., and Klemperer, L., 2008, Discontinuous and diachronous evolution of the Main Ethiopian Rift : Implications for development of continental rifts: Earth and Planetary Science Letters, v. 265, p. 96–111, doi:10.1016/j.epsl.2007.09.038.

Keranen, K., Klemperer, J., Julia. J, Lawrence, J.F., and Nyblade, A.A., 2009, The Main Ethiopian Rift: a Narrow Rift in a Hot Craton? Geochemistry, Geophysics, Geosystems, v. 10, Q0AB01, doi:10.1029/2008GC002293.

Kim, S., Nyblade, A.A., Rhie, J., Baag, C.E., and Kang, T.S., 2012, Crustal S-wave velocity structure of the Main Ethiopian Rift from ambient noise tomography: Geophysical Journal International, v. 191, p. 865–878, doi:10.1111/j.1365-246X.2012.05664.x.

Kogan, L., Fisseha, S., Bendick, R., Reilinger, R., Mcclusky, S., King, R., and Solomon, T., 2012, Lithospheric strength and strain localization in continental extension from observations of the East African Rift: Journal of Geophysical Research, v. 117, p. B03402, doi:10.1029/2011JB008516.

Korostelev, F. et al., 2015, Magmatism on rift flanks: Insights from ambient noise phase velocity in Afar region: Geophysical Research Letters, v. 42, p. 2179–2188, doi:10.1002/2015GL063259.

Kurkura, K., 2010, Geological and geochemical variations in Mid-Tertiary Ethiopian Flood Basalt Province, Maychew, Tigray Region, Ethiopia: Department of Earth Science, College of Natural and Computational Sciences, v. 2, p. 4–25.

Levshin, A.L., Yanovskaya, T.B., Lander, A. V, Buckchin, B.G., Barmin, M.P., and Ratnikova, L.I., 1989, In: Keilis-Borok, V.I. (Ed.),: Seismic Surface Waves in a Laterally Inhomogeneous Earth. Kluwer, Norwell, Mass,.

Macgregor, D., 2015, History of the development of the East African Rift System : A series of interpreted maps through time: Journal of African Earth Sciences, v. 101, p. 232–252, doi:10.1016/j.jafrearsci.2014.09.016.

Mackenzie, G.D., Thybo, H., and Maguire, P.K.H., 2005, Crustal velocity structure across the Main Ethiopian Rift : results from two-dimensional wide-angle seismic modelling: Geophysical Journal International, v. 162, p. 994–1006, doi:10.1111/j.1365-246X.2005.02710.x.

Maguire, P.K.H. et al., 2006, Crustal structure of the northern Main Ethiopian Rift from the EAGLE controlled-source survey ; a snapshot of incipient lithospheric break-up: Geological Society, London, Special Publications, v. 259, p. 269–291.

Maguire, P.K.H. et al., 2003, Geophysical Project in Ethiopia Studies Continental Breakup: EOS, Transactions of the American Geophysical Union, v. 84, p. 337–340, doi:10.1029/2003EO350002.

Maguire, P.K.H., and SEIS-UK, 2002, A new dimension for UK seismology: Astronomy and Geophysics, v. 42, p. 23 – 25.

Makris, J., and Ginzburg, A., 1987, The Afar Depression: transition between continental rifting and sea-floor spreading: Tectonophysics, v. 141, p. 199–214.

Mammo, T., 2013, Crustal Structure of the Flood Basalt Province of Ethiopia from Constrained 3-D Gravity Inversion: Pure and Applied Geophysics, v. 170, p. 493–744, doi:10.1007/s00024-013-0663-0.

Manighetti, I., King, G.C.P., and Gaudemer, Y., 2001, Slip accumulation and lateral propagation of active normal faults in Afar: Journal of Geophysical Research, v. 106, p. 13,667-13,69.

Mohr, P., 1983, Ethiopian flood basalt province: Nature, v. 303, p. 577–584.

Mohr, P.A., 1970, Ethiopian Rift and Plateaus: Some Volcanic Petrochemical Differences: Journal of Geophysical Research, v. 76, p. 1967–1983.

Mohr, P., Mitchell, J.G., and Raynolds, R.G.H., 1980, Quaternary Volcanism and Faulting at O ' A Caldera , Central Ethiopian Rift: Bull. Volcanol, v. 43–1.

Mohr, P.A., and Potter, E.C., 1976, The Sagatu Ridge Dike Swarm, Ethiopian Rift Margin: Journal of Volcanology and Geothermal Research, v. 1, p. 55–71.

Mohr, P., and Zanetin, B., 1988, The Ethiopian Flood Basalt Province: J. D. Macdougall (ed.), ContinenJal Flood Basalts, p. 63–110.

Muluneh, A.A., Cuffaro, M., and Doglioni, C., 2014, Tectonophysics Left-lateral transtension along the Ethiopian Rift and constrains on the mantle-reference plate motions: Tectonophysics, doi:http://dx.doi.org/10.1016/j.tecto.2014.05.036.

Muluneh, A.A., Kidane, T., Corti, G., and Keir, D., 2018, Constraints on fault and crustal strength of the Main Ethiopian Rift from formal inversion of earthquake focal Mechanism data: Tectonophysics, doi:10.1016/j.tecto.2018.03.010.

Nyblade, A., 2000, Seismic Investigation of Deep Structure Beneath the Ethiopian Plateau and Afar Depression: International Federation of Digital Seismograph Networks, doi:https://doi.org/10.7914/SN/XI_2000.

Peccerillo, A., Donati, C., Santo, A.P., Orlando, A., Yirgu, G., and Ayalew, D., 2007, Petrogenesis of silicic peralkaline rocks in the Ethiopian rift: Geochemical evidence and volcanological implications: Journal of African Earth Sciences, v. 48, p. 161–173, doi:10.1016/j.jafrearsci.2006.06.010.

Penn State University, 2004, AfricaArray: International Federation of Digital Seismograph Networks, doi:https://doi.org/10.7914/SN/AF.

Phạm, T.S., Tkalčić, H., Sambridge, M., and Kennett, B.L.N., 2018, Earth's correlation wavefield: Late coda correlation.: Geophysical Research Letters, v. 45, p. 3035–3042, doi:https://doi.org/10.1002/2018GL077244.

Piccirillo, E.M., Justin-Visentin, E., Zanettin, B., Joron, J.L., and Treuil, M., 1979, Geodynamic evolution from plateau to rift: major and trace element geochemistry of the central eastern Ethiopian Plateau volcanics: N. Jb. Geol. Palaont. ABH, v. 158, p. 139–179.

Ray, A., and Key, K., 2012, Bayesian inversion of marine CSEM data with a trans-dimensional self parametrizing algorithm: Geophysical Journal International, v. 191, p. 1135–1151, doi:10.1111/j.1365-246X.2012.05677.x.

Rochette, P., Tamrat, E., and Fe, G., 1998, Magnetostratigraphy and timing of the Oligocene Ethiopian traps: Earth and Planetary Science Letters, v. 164, p. 497–510.

Rogers, N.W., 2006, Basaltic magmatism and the geodynamics of the East African Rift System. In: The Afar Volcanic Province within the East African Rift System (G. Yirgu, C.J. Ebinger and P.K.H. Maguire, eds): Geological Society, London, Special Publications, v. 259, p. 77–93.

Rooney, T., Furman, T., Bastow, I., Ayalew, D., and Yirgu, G., 2007, Lithospheric modification during crustal extension in the Main Ethiopian Rift: Journal of Geophysical Research, v. 112, p. B10201, doi:10.1029/2006JB004916.

Rooney, T.O., Furman, T., Yirgu, G., and Ayalew, D., 2005, Structure of the Ethiopian lithosphere : Xenolith evidence in the Main Ethiopian Rift: Geochimica et Cosmochimica Acta, v. 69, p. 3889–3910, doi:10.1016/j.gca.2005.03.043.

Ryberg, T., Muksin, U., and Bauer, K., 2016, Ambient seismic noise tomography reveals a hidden caldera and its relation to the Tarutung pull-apart basin at the Sumatran Fault Zone , Indonesia: Journal of Volcanology and Geothermal Research, v. 321, p. 73–84, doi:10.1016/j.jvolgeores.2016.04.035.

Sembroni, A., Faccenna, C., Becker, T.W., Molin, P., and Abebe, B., 2016, Long-term, deep-mantle support of the Ethiopia-Yemen Plateau: Tectonics, v. 35, p. 469–488, doi:10.1002/2015TC004000.Received.

Shapiro, N.M., and Campillo, 2004, Emergence of broadband Rayleigh waves from correlations of the ambient seismic noise: Journal of Geophysical Research, v. 31, p. L07614, doi:10.1029/2004GL019491.

Souriot, T., and Brun, J.., 1992, Faulting and block rotation in the Afar triangle:the Danakil "crank arm" model: Geology, v. 20, p. 911–914.

Stuart, G.W., Bastow, I.D., and Ebinger, C.J., 2006, Crustal structure of the northern Main Ethiopian Rift from

receiver function studies: Geological Society, London, Special Publications, v. 259, p. 253–267, doi:10.1144/GSL.SP.2006.259.01.20.

Stuart, G., Hammond, J., Kendall, M., and Keir, D., 2011, Afar Rift Consortium.:

Tilmann, F.J., Sadeghisorkhani, H., and Mauerberger, A., 2020, Another look at the treatment of data uncertainty in Markov chain Monte Carlo inversion and other probabilistic methods: Geophysical Journal International,.

USGS, A.S.L., 1988, Global Seismograph Network (GSN - IRIS/USGS): International Federation of Digital Seismograph Networks, doi:https://doi.org/10.7914/SN/IU.

Wessel, P., Luis, J., Uieda, L., and Oceanic, N., 2019, The Generic Mapping Tools Version 6: Geochemistry, Geophysics, Geosystems, doi:10.1029/2019GC008515.

White, R., and Mckenzie, D., 1989, Magmatism at Rift Zones : The Generation of Volcanic Continental Margins and Flood Basalts: Journal of Geophysical Research, v. 94, p. 7685–7729.

Woldegabriel, G., Aronson, J., and Walter, R.C., 1990, Geology, Geochronology, and Rift Basin Development in the central sector of the Main Ethiopia Rift: Geological Society of America Bulletin, v. 102, p. 439–458.

Woldegabriel, G., Heiken, G., White, T.D., Hart, W.K., and Renne, P.R., 2000, Volcanism, tectonism, sedimentation, and the paleoanthropo- logical record in the Ethiopian Rift System: Geological Society of America,.

Wolfenden, E., Ebinger, C., Yirgu, G., Deino, A., and Ayalew, D., 2004, Evolution of the northern Main Ethiopian rift : birth of a triple junction: Earth and Planetary Science Letters, v. 224, p. 213–228, doi:10.1016/j.epsl.2004.04.022.

Wright, T.J., Ebinger, C., Biggs, J., Ayele, A., Yirgu, G., Keir, D., and Stork, A., 2006, Magma-maintained rift segmentation at continental rupture in the 2005 Afar dyking episode: Nature, v. 442, p. 291–294, doi:10.1038/nature04978.

Yirgu, G., Ebinger, C.J., and Maguire, P.K.H., 2006, The Afar volcanic province within the East African Rift System: introduction: Geological Society of London, v. 259, p. 1–6, doi:10.1144/GSL.SP.2006.259.01.01.

Young, M.K., Rawlinson, N., and Bodin, T., 2013, Transdimensional inversion of ambient seismic noise for 3D shear velocity structure of the Tasmanian crust: v. 78.

Zanettin, B., 1993, On the evolution of the Ethiopian volcanic province. In: Geology and Mineral Resources of Somalia and Surrounding Regions. Abbate, E. et al. (Eds.). Ist. Agron: Oltremare, Firenze, Relaz. Monogr. Agrar. Subtrop. Trop., Nuova Ser, v. 113, p. 279–310.

Zanettin, B., Gregnanin, A., Justin-Visentin, E., Nicoletti, E., Petrucciani, C., Piccirillo, E.M., and Tolomeo, L., 1974, Migration of the Oligocene- Miocene ignimbritic volcanism in the Central Ethiopan Plateau: NGB Geol Palaeo Mh H, v. 9, p. 567–574.

Zanettin, B., and Justin-Visentin, E., 1975, Tectonical and volcanological evolution of the western Afar margin (Ethiopia), In: Pilger A, Roesler EA (eds) Afar depression of Ethiopia.: Schweizerbart, Stuttgart, p. 300 – 309.

Zanettin, B., and Justin-Visentin, E., 1974, The volcanic succession in central Ethiopia:The volcanics of western Afar and Ethiopian rift margins: Mem Ist Min Univ Padova, v. 31, p. 1–19.

Zanettin, B., Justin, V.E., Nicoletti, E., and Piccirillo, E.M., 1980, Correlations among Ethiopian volcanic formations with special references to the chronological and stratigraphical problems of the "Trap Series": Atti Convegni Acc Lincei Roma, v. 47, p. 231–252.